PAPER

Check for updates

Insights into the metal retention role in the antibacterial behavior of montmorillonite and cellulose tissue-supported copper and silver nanoparticles†

Farzaneh Noori,[a] Armelle Tchoumi Neree,[b] Meriem Megoura,[ab] Mircea Alexandru Mateescu (ID) *[ab] and Abdelkrim Azzouz (ID) *[a]

The role of the retention strength of Cu^0 and Ag^0 nanoparticles on the induced antibacterial properties of montmorillonite and cellulose-supported polyol dendrimer was comparatively investigated. An unprecedented approach involving X-ray photoelectron spectroscopy, thermal analyses, and surface charge measurements allowed correlating the host–matrix features to the different antibacterial activities of Cu^0 and Ag^0 nanoparticles against both the bacterial strains. Optimal metal–matrix interactions appear to favor high dispersion of both metal particles and material grains, thereby improving the contact surface with the cultivation media. This was explained in terms of hydrophilic character and judicious compromise between the metal retention by the host–matrix and release in the impregnating media. Competitive Lewis acid–base interactions appear to occur between MNP, solid surface and liquid media. These findings are of great importance, providing a deeper understanding of the antibacterial activity of metal-loaded materials. This opens promising prospects for vegetal fibers and clay-supported drugs to treat dermatological and gastro-intestinal infections.

1. Introduction

Overuse of conventional antibiotics has led to pathogenic bacteria adaption and rise of resistance, which has been found to be a direct cause of a series of outbreaks of infectious diseases.[1] This has become a major medical issue that has imposed a great challenge to be addressed.[2] Some metal nanoparticles (MNPs) can behave as potential surrogates for organic antibiotics, given the well-known toxicity of heavy metals in certain concentrations in aqueous media. Metals are known as metabolism disturbing agents, some of them being harmful for animals and humans.[3] Certain zero-valent metals (metal-zero) such as silver in high dispersion state have long been used for treating skin bacterial infections.[4] Nanoparticles of gold, zinc, and titanium have showed high bioactivity. In this context, silver (Ag) and copper (Cu) are also promising nano-particles that have shown broad-spectrum activity against many species of Gram-positive and Gram-negative bacteria.[5–11] High antibacterial activity against pathogens has already been reported for finely dispersed MNP[12] and more particularly AgNPs, which

appears to generate free radicals that inhibit microbial growth.[13] Reportedly, eco-friendly and cost-effective cotton fabric-based composite materials doped with copper oxide have shown anti-bacterial action against *Staphylococcus epidermis* and *Escherichia coli*.[14] Preliminary unpublished tests have provided arguments that metal-loaded polyhydroxylic matrices act as antibacterial agents.[15]

These performances have often been explained in terms of the contribution of the antibacterial properties of metal without sufficient emphasis on metal dispersion. In spite of the wide literature reported in this regard, the effect of the interactions occurring between the host–matrix and both MNPs on the infected media has scarcely been tackled so far. Furthermore, the role of metal retention strength in the antibacterial activity that has never been evaluated and still remains to be elucidated has been undertaken in the present study.

MNPs have a strong tendency to aggregate into bulky inactive clusters.[16] So far, a wide variety of metal-loaded materials with antibacterial activity have been synthesized.[17] Both zero-valent and cationic metal forms are known to behave as Lewis acids, and can interact with basic chemical groups. Polyols and poly-amines bear specific chemical groups that confer them chelating and stabilizing properties for metals.[18] Besides, unavoidable interparticle H-bridges interactions often lead to a compacted structure and enhanced metal encapsulation that impede direct metal interaction with the infected area, thereby reducing their antibacterial activity. MNP dispersion and

[a]*Chemistry Department, Nanoqam, Université du Québec à Montréal, QC, H3C 3P8, Canada. E-mail: mateescu.m-alexandru@uqam.ca; azzouz.a@uqam.ca; Fax: +1 514 987 4054; Tel: +1 514 987-4319; +1 514 987 3000 ext. 4119*

[b]*CERMO-FC Center, Université du Québec à Montréal, QC, H3C 3P8, Canada*

stabilization on inorganic solid surfaces and/or specifically functionalized polymers provide metal-loaded inorganic–organic materials that allow to overcome this significant drawback.[19] Their synthesis has become one of the main targets of the present research.

Such a novel class of solid antibacterial agents are supposed to act as an MNP reservoir. A wide variety of materials have been more or less successfully tested as host–matrices for MNP so far, and ample literature has been reported in this direction. Nevertheless, the use of natural and organically-modified clay minerals has barely been investigated. These materials display high surface-to-volume ratios, chemical stability, thermal resistance, non-toxicity, and recyclability.[20] Among these, smectite-type sodium montmorillonite (NaMt) is of particular interest due to its natural abundance, cost effectiveness, chemical inertness, sorptive capabilities, large specific surface area,[21] and even beneficial medicinal effects.[5,22] This crystalline alumino-silicate is also known to be harmless for human health and biodiversity, and has already found some applications in biochemical and biomedical fields. Successful attempts against bacteria were already achieved using other clay minerals such as allophane and imogolite doped with metals such as Ag, Cu, Co, and Zn.[13,23,24] Attempts have also been achieved using functionalized clay minerals and vegetal fibers for the dispersion of silver and copper ions.[25]

The adsorptive properties of NaMt are governed by a large specific surface area bearing net negative charges and both in-plane and out-of-plane silanol groups. The latter are known to act as Lewis bases and effective chelating groups for metals due to the electron pair of the oxygen atoms. Additional hydroxyl groups can be brought by clay intercalation with dendritic polyols[26–29] or by the direct use of polyhydroxylic polymers.

Deeper insights into metal–matrix interaction (MMI) were achieved herein through a comparative study of the antibacterial activity of the two metals (copper and silver) in both cationic and zero-valency dispersion form on a clay mineral, a vegetal polymer, and their combination against two pathogenic bacteria strains. Diverse analysis techniques are expected to provide complementary data for demonstrating the proof-of-concept that the antibacterial activity requires optimal MMI, *i.e.*, a judicious compromise between strong metal retention by the host–matrix but a paradoxically easy metal release due to a high contact surface with the cultivation media. This is a comprehensive approach that is expected to allow the tailoring of optimal interactions with the MNP-matrix by modifying the surface type and the number of hydroxyl groups of the incorporated organic moiety. This should provide valuable data for correlating the influence of the metal retention strength and the release velocity of the induced antibacterial activity. This is a new concept that opens new prospects for the controlled release of diverse medicinal substrates.

2. Experimental

2.1. Materials preparation and polyol dispersion

All chemicals were of analytical grade and used without previous purification. Crude bentonite (Sigma-Aldrich, Oakville, Canada), sodium chloride (NaCl) (ACP chemicals, Montreal, Canada), copper acetate $(Cu(CH_3COO)_2)$ (Fisher chemicals, Ottawa, Canada), silver nitrate $(AgNO_3)$ (Fisher chemicals), sodium borohydride 98% $(NaBH_4)$ (Acros organics, Ottawa, Canada), copper nitrate $(Cu(NO_3)_2)$ (Anachemia VWR company, Montreal, Canada), Boltorn™ H20 (Perstorp, Malmo, Sweden), absolute methanol (MeOH) (Sigma-Aldrich), and toluene (Sigma-Aldrich) were used. All the experiments were performed in distilled water. Cellulose tissue (gauze) denoted as CT was purchased from PJC, Canada.

Sodium-montmorillonite (NaMt) was prepared by combined ion-exchange and the purification of crude bentonite (Aldrich) in an aqueous NaCl solution using an effective procedure fully described elsewhere.[30,31] NaMt (200 mg) was immersed in a methanol/water mixture containing 200 mg of the Boltorn™ H20 polyol dendrimer (41.2 : 58.8 v/v ratio) under continuous stirring for 1 h at 40–60 °C, resulting in H20–NaMt organoclay, which was dried overnight in a freeze-drying device. Similarly, the impregnation of a CT patch of 1×0.5 mm^2 surface in 20 mL of an aqueous solution of 0.01 mol L^{-1} Boltorn™ H20 at room temperature (RT) for 1 h resulted in dendrimer dispersion into a H20–CT composite.

2.2. Metal dispersion on the composite supports

0.2 g of NaMt or H20–NaMt was slowly mixed in a 50 mL beaker with 15 mL (33.33% and 66.66% toluene/water) aqueous solution with a metal salt concentration of 0.12 mol L^{-1} Cu $(CH_3COO)_2$ or $(AgNO_3)$ under vigorous stirring for 2 h. For comparison, some antibacterial tests were only performed with the resulting Cu^{2+}/NaMt@H20 and Ag^+/NaMt@H20. Both cation-loaded organoclay suspensions were treated by the dropwise addition of 10 mL aqueous solution of $NaBH_4$ (0.2 mol L^{-1}) for 15 min under a nitrogen stream at ambient conditions. The resulting metal-zero-loaded clay minerals $(Cu^0/NaMt$ and $Ag^0/NaMt)$ and organoclays $(Cu^0/H20–NaMt$ and $Ag^0/H20–NaMt)$ were repeatedly washed with distilled water to eliminate the excess of Cu^{2+} and Ag^+ salts and then dried overnight. Further, metal-loaded H20–CT samples were obtained by dissolving 0.8 g of $AgNO_3$ or 1.24 g of $Cu(NO_3)_2$ in 30 mL of distilled water and adding with 1 g and 1.5 g of $NaBH_4$, respectively. Cu^{2+} and Ag^+ reduction into Cu^0 and Ag^0 nanoparticles (AgNP and CuNP) was achieved under stirring for 5–6 h at RT under a nitrogen stream to prevent MNP oxidation. The resulting Ag^0/H20–CT and Cu^0/H20–CT samples were dried overnight at RT in a sealed enclosure with dry O_2-free nitrogen dried with NaOH pellets.

2.3. Material characterization

The basicity and hydrophilic character of the as-prepared samples were assessed in terms of the carbon dioxide (CO_2) retention capacity (CRC) through Thermal Programmed Desorption (TPD) and moisture content by thermogravimetric analysis. (TGA). The basicity of diverse materials is commonly defined as the surface affinity toward an acidic gas such as CO_2. This is herein assessed by TPD in terms of the CRC or total basicity, which accounts for the total amount of desorbed CO_2

within the investigated temperature range. The basic strength accounts for CO_2 retention strength, and is proportional to the CO_2 desorption temperature.[30,32–46] For this purpose, 45–50 mg of each material sample was prone to previous saturation with dry and O_2-free CO_2 and then to a 5 °C min^{-1} heating rate from 20 °C to a given temperature threshold under 5 mL min^{-1} nitrogen stream. This temperature threshold was evaluated as the stability range through TGA by means of a TA Instruments TGA (Q500)/discovery MS equipment. This was achieved by heating 4–7 mg samples in a platinum (Pt) pan in the temperature range of 20–500 °C at a 10 °C min^{-1} heating rate under a 30 mL min^{-1} dry argon stream. The particle morphology was screened by Scanning Electron Microscopy (SEM) using a JEOL JCM-6000 PLUS instrument on samples spread as a powder on conductive double adhesive carbon tapes at 1.0 kV voltage for non-conductive samples and 15 kV for metal-containing materials (conductive). Deeper insights into MNP incorporation were achieved through Transmission Electron Microscopy (TEM) and energy-dispersion X-ray fluorescence (EX-XRF) by means of the JEOL JEM-2100F equipment (with an accelerating voltage of 200 kV) coupled to an EDAX X-ray fluorimeter. The samples were previously dispersed in methanol and dried on holey carbon-coated Ni grids. The ED-XRF spots were denoted as eds1 and eds1. This notation arises from a shortening of this acronym into Energy-Dispersive Spectroscopy (EDS). Additional analyses were performed by X-ray diffraction (XRD) in 2-theta range of 10–80° (XRD D8 Advance device and CuK$_{alpha}$ radiation at 1.5406 Å), X-ray photo-electron spectroscopy (XPS) XPS of 7800 × 300 μm spots (Axis-Ultra instrument, Kratos Analytical Ltd, UK), and a monochromatic Al-based X-ray source (260 watts in constant pass energy mode in two 160 eV and 1 eV steps).

2.4. Antibacterial tests

The antimicrobial behavior of the as-prepared samples was evaluated by the diffusion and inhibition zone tests toward *Bacillus subtilis 168* and *Escherichia coli DH5α* bacterial strains. Almost similar wall structures and behavior were reported between Gram+ pathogenic and non-pathogenic strains.[47,48] Non-pathogenic strains also appear to influence the intestinal homeostasis through anti-inflammatory responses and mild inflammation.[49] This justified their use herein for assessing the MNP toxicity on the bacteria integrity and providing the proof-of-concept of the key role of metal–matrix interaction on the antibacterial behavior. Copper and silver ions have the capacity to kill bacteria by destroying their walls and membranes in the presence of both pathogenic and non-pathogenic strains.

The assay is a semi-quantitative method where 5 mg metal-loaded clay materials or 1×0.5 mm^2 CT-based samples were inoculated in Petri dishes pre-seeded by approximately 74×10^6 colony forming units CFU mL^{-1} of each bacterial strain with a cell optical density of 0.5 at 600 nm. Negative controls were included in each assay. All experiments were performed in triplicate involving three independent growth cultures with at least two technical replicates for each growth culture. After 24 h of incubation at 37 °C, the antibacterial activity was assessed through measurements of the inhibition zone diameter (IZD).

The effect of the material amount on the IZD values was investigated by inoculating 1–9 mg of the metal-loaded clay materials in both series of pre-seeded Petri dishes.

3. Results and discussion

3.1. Metal dispersion on unmodified supports

CuNP and AgNP dispersion into polyol-based matrices in the presence of NaBH$_4$ was first noticed by color changes from blue to black for Cu^{2+} conversion into Cu^0 and from colorless to light grey for Ag$^+$ conversion into Ag^0 (Fig. S1†). Almost similar color change was observed for the MNP dispersion in the H20–CT-based samples (Fig. S2†). Metal incorporation was confirmed by the visible modification of the morphology of the surface of the host material. Preliminary observations through optical microscopy revealed a transition from a clean and almost soft surface of the NaMt to the appearance of grains on the surfaces of both Cu^0/NaMt and Ag^0/NaMt (Fig. S3†) and on the CT-based materials (Fig. S4†).

SEM analysis revealed larger amounts of spheroidal grains smaller than 100 nm and fewer quantities of crystalline rods of residual metal salt on both the MNP-loaded NaMt (Fig. 1(a1–a3)) as compared to the CT samples (Fig. 1(a4–a6)). The CT samples showed non-uniform dispersion of the spheroidal grains, suggesting a weak CT–MNP interaction. The relatively high amount of Ag salt needles must originate from the lower capacity of silver to undergo redox processes, indicating a lower amount of incorporated Ag^{0}NP. Thus, Ag-based materials are expected to exhibit a weaker antibacterial activity compared to their Cu-counterparts; this will be examined further.

The rise of metal-loaded dendrimer scales not anchored on the CT surface may be due to weak CT interaction with the dendrimer H20, if any (Fig. 2). The most plausible explanation resides in a deficiency in the OH groups on the CT surface. This is expected to rather promote [H20:H20] H-bridges and [H20:MNP] attraction forces at the expense of binary [CT:H20] and ternary [CT:H20:CuNP] interactions within the polymer entanglement.

3.2. Effect of polyol incorporation on metal dispersion

Dendrimer H20 incorporation induced the total disappearance of such crystalline rods on Cu^0/H20–CT. Their persistence in trace amounts on Ag^0/H20–CT confirms the lower amount of Ag^0 particles. This beneficial effect of dendrimer H20 on MNP dispersion appears to markedly mitigate this drawback, presumably through a previous dispersion of metal cations even before reduction. This was followed by instant entrapment and stabilization of the rising MNP within the dendrimer entanglement, resulting in a pronounced improvement of the metal dispersion on H20–NaMt (Fig. 3). This higher capacity of H20–NaMt to host MNP should arise from the contributions of the OH groups of both the clay surface and the dendrimer branches in the formation of ternary [NaMt–polyol–MNP] interactions.

This result is of great importance because it provides evidence that the presence of OH groups on the surface of the support is an essential requirement for high MNP dispersion.
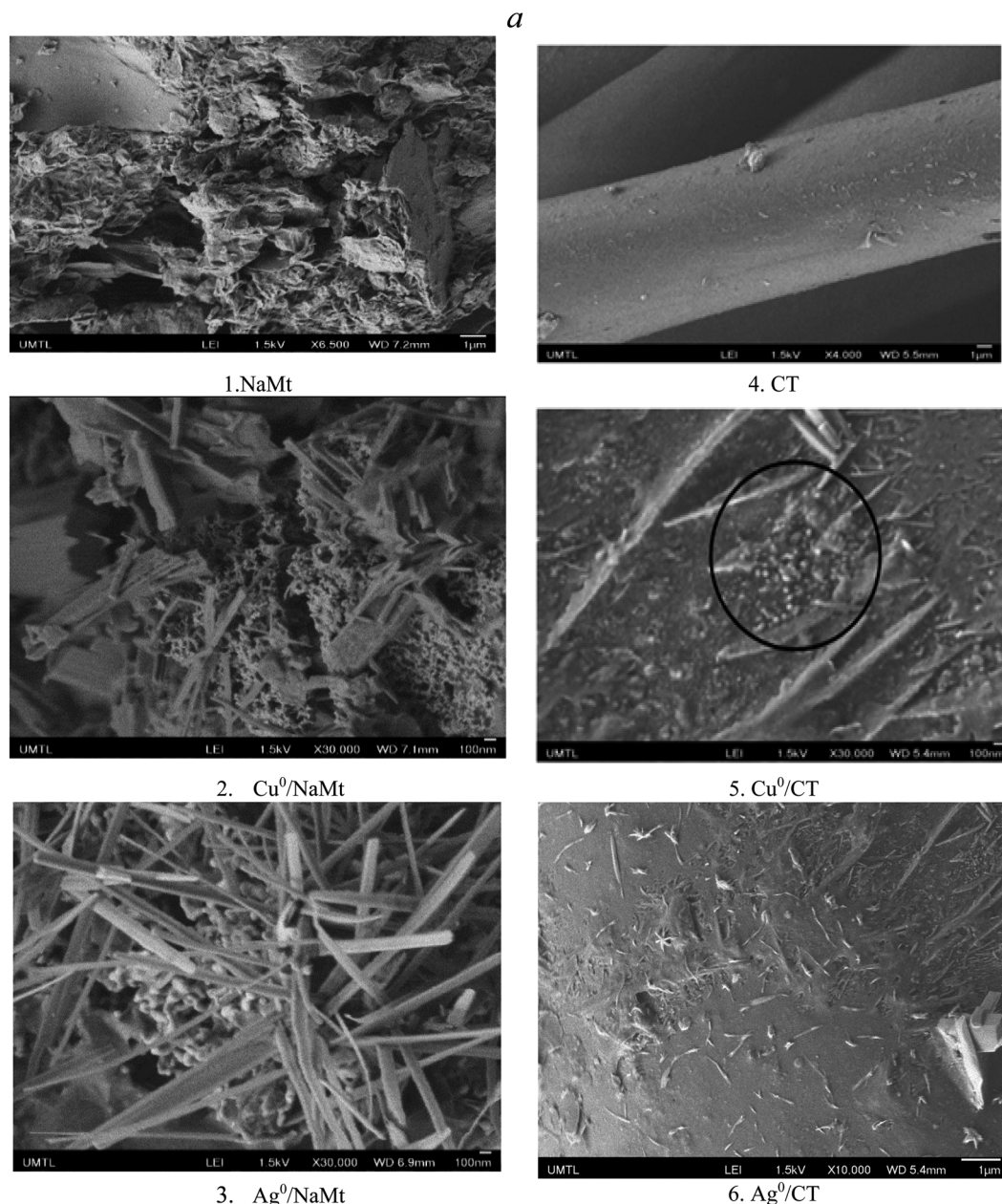
a

1. NaMt

4. CT

2. Cu⁰/NaMt

5. Cu⁰/CT

3. Ag⁰/NaMt

6. Ag⁰/CT

Fig. 1 SEM images of NaMt, CT, and their metal-loaded counterparts.

Deeper TEM insights on the H20–NaMt samples revealed a higher copper dispersion as reflected by a much lower average particle diameter not exceeding 5.5 nm as compared to silver (30 nm) (Fig. 4). Closeup analysis on eds2 spots on the grey surface between the black stains through EX-XRF revealed the presence of metal sub-nanometric particles (MSNP) in Cu^0/ H20–NaMt. No MSNP were detected in Ag^0/H20–NaMt, thereby confirming its much weaker dispersion capacity as compared to that of copper.

Attempts to assess the size of copper sub-nanometric particles (CuSNP) using the ImageJ software on metal-free blank samples and Cu–H20–NaMt resulted in average particle diameter values ranging from 0.08 to 0.22 nm. The expected face-centered cubic (fcc) symmetry and 0.74 compactness factor of Cu^0 suggest the occurrence of CuSNP with less than 5 copper atoms, given that one 0.5 nm particle and one 1 nm particle are supposed to have *ca.* 5 and 38 Cu^0 atoms, respectively.[28] Calculations based on ED-XRF measurements on the two samples of each metal-loaded composite (Fig. S5 and S6†) gave O/Cu^0 atom ratio ranging from 1.4 to 1.7 in eds1 spot and from 3.8 to 9.6 in eds2 spot. For comparison, the average O/Cu^0 value was found to be *ca.* three folds higher than that of the O/ Ag^0 atom ratio, thereby explaining the higher antibacterial activity of Cu^0/H20–NaMt in spite of its lower Cu^0 content, as expressed in terms of the $Cu/(Si + Al + O)$ mole ratio of 0.18 *versus* 0.24 for the $Ag/(Si + Al + O)$ value. Here, the metal

Fig. 2 SEM image of $Cu^0/H20-CT$.

particle size appears to play a key role, provided that the material particle size is sufficient to afford optimal surface contact with the aqueous media.

3.3. Changes in clay surface basicity

The involvement of the OH groups in metal stabilization is expected to induce changes in the hydrophilic character and basicity of the host materials. Insights through TPD revealed the occurrence of at least four desorption peaks for NaMt. This should account for four basicity strengths, namely, weakly (below 100 °C), medium (between 100 and 250 °C), medium-to-strong (between 300 and 450 °C), and strong basicity (between 450 and 550 °C). The slight shift of the desorption peak from 60–200 °C toward higher temperatures (170–220 °C) was noticed from bentonite to NaMt (Fig. S7a†). This indicates a slight enhancement and strengthening of the surface basicity, most likely due to the removal of acidic silica phases (quartz, sand, cristobalite). This agrees with the slight increase in the CRC value from 2101 to 2261 μmol g^{-1} after bentonite purification (Table 1).

Silica phase removal was supported by the marked depletion of the XRD lines assigned to quartz (denoted as Q) after bentonite purification and the presence of the main XRD lines of crystalline silica in the pattern of the residual ash (Fig. S8†).
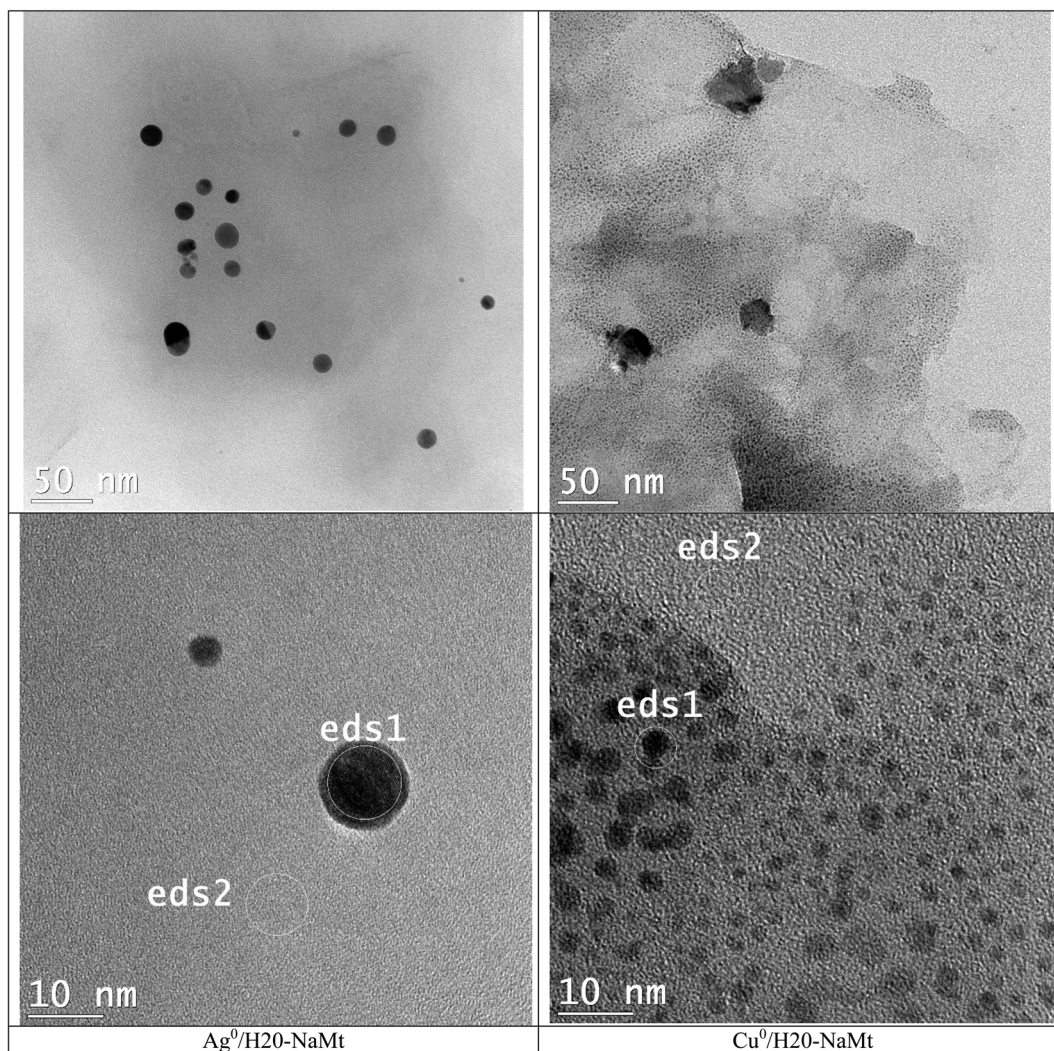

Fig. 3 TEM images of metal-loaded H20−NaMt composites. The ED-XRF spots were denoted as eds1 and eds1, as previously defined.
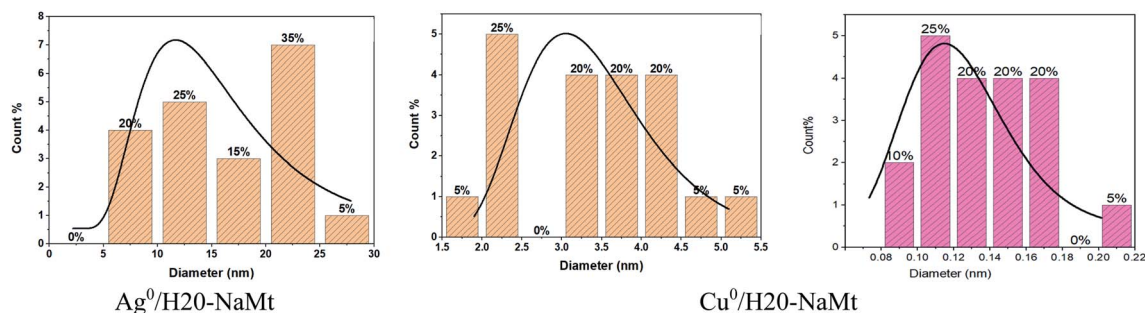
Paper

Fig. 4 Average particle diameter of metal-loaded H20−NaMt composites as assessed by the ImageJ software.

The shift in the 001 XRD line from a 2θ value of $7.357°$ for bentonite to $9.142°$ for NaMt indicates a decrease in the inter-layer spacing. This must originate from the replacement of bulky impurity particles and diverse cations by Na^+. This was confirmed by a noticeable sharpening and increased intensity of the main XRD lines of NaMt, which is a special feature of the homo-ionic form of montmorillonite and almost perfect parallel arrangements of the clay sheets. This somehow explains the lower moisture content value observed for NaMt compared to bentonite, given that the Na^+ cation has a lower polarizing power and thereby weaker capacity to attract water molecules than multivalent cations. MNP incorporation in NaMt induced a marked decrease in the CRC from 2261 μmol g^{-1} down to 662 μmol g^{-1} for Ag^0/NaMt and 55.5 μmol g^{-1} for Cu^0/NaMt, providing clear evidence of the occurrence of competitive interaction of CO_2 and metal with the clay surface. Here, the metal dispersion must involve at least two kinds of interactions. Some MNP interactions occur with the lattice oxygen atoms (−Si−O−Si− with strong Lewis basicity), while others should take place with the OH groups of both in-plane silanols and out-of-plane Si−OH of the surface.[50]

3.4. Changes in the CT surface basicity

The CT-based samples exhibited much lower surface basicity as compared to clay materials. TDP measurements for untreated cellulose tissue revealed no CO_2 desorption peak in the temperature range of 20–100 °C. Polyol incorporation induced a marked change in the TPD profile, reflected by the appearance of a wide desorption peak between 20 and 110 °C (Fig. S7b†). This accounts for a rise in the weakly basic adsorption sites, most likely amphoteric to slightly basic OH groups, belonging to the inserted polyol dendrimer. As expected, OH groups were found to dramatically decline after CuNP insertion and totally disappear after AgNP incorporation. This is a confirmation of the occurrence of [−HO:MNP] interaction. This pronounced OH decay accounts for stronger [AgNP:OH−] interaction and a stronger entrapment as compared to CuNP, and allows predicting a less intense Ag^0 release and weaker antibacterial activity as compared to CuNP.

3.5. Changes in the hydrophilic character

The hydrophilic character is expected to favor the material dispersion in the aqueous media, while the antibacterial activity must be strong dependent on the material affinity toward aqueous media where the bacteria naturally grow. This affinity toward water can be evaluated by TGA,[51] which revealed a single and small weight loss (WL) of at most 1.0–1.2% for NaMt between 20 and 120 °C, corresponding to reversible dehydration (Fig. S9a,† pattern 1). Rehydration was found to revive the WL as supported by similar TGA patterns obtained after repeated TGA analysis–rehydration cycles. The total absence of other weight losses at higher temperature and more particularly of dehydroxylation (2-Si−OH → Si−O−Si− + H_2O) provided evidence that NaMt is stable throughout the entire range of temperatures investigated.

A noticeable decay in dehydration was noticed after CuNP incorporation, as reflected by the pattern flattening with a WL not exceeding 0.7–1.0% in the temperature range if 20–120 °C (pattern 2). This is concordance with the depletion of unoccupied OH groups due to the rise of competitive [−HO: metal] interaction, as previously stated. MNP insertion into NaMt also

Table 1 CO_2 retention capacity (μmol g^{-1}) and weight loss for the synthesized materials

Material	TPD measurements	TGA measurements[b]	
	CRC^a (μmol g^{-1})	Temperature (°C)	Weight loss (%)
Bentonite	2101	—	—
Residual ash	1752	—	—
NaMt	2261	20–140	1.0–1.2
Cu^0/NaMt	55.5	20–140	0.5–0.6
		140–480	6.6
Ag^0/NaMt	662	20–90	1.9
		90–470	9.4
CT	—	47–130	0–0.1
H20–CT	38.4	47–185	0.275
Cu^0/CT	—	43–190	8.25
Ag^0/CT	—	47–200	8.74
Cu^0/H20–CT	14.5	32–200	4.675
Ag^0/H20–CT	5.6	40–200	8.525

[a] CRC: CO_2 retention capacity. [b] TGA measurements were performed between 25 and 700 °C for clay-based samples and between 25 and 200 °C for CT-based materials. The weight loss measured for each material within the lowest temperature range accounts for dehydration and provides the moisture content.

gave rise to a marked endothermic process at *ca.* 140–480 °C for Cu^0/NaMt and at 90–470 °C for Ag^0/NaMt with a 6.6% and a 9.4% WL, respectively (Table 1). A possible explanation could be delayed and slow moisture release from the internal surface due to weak moisture diffusion across a compacted structure of the MNP-loaded clay mineral.[52] Another WL was noticed at 470–480 °C and could be related to the dehydroxylation of terminal metal–OH groups of the possible metal oxide particles. The latter may unavoidably be produced during the synthetic procedure through slight metal oxidation when contacted with air. Both WL were found to shift toward lower temperatures but with higher WL values in Ag^0/NaMt, indicating a slightly higher hydrophilic character. This suggests lesser formation of AgNP and [–HO:Ag^0] interaction, and thereby, more available hydrophilic OH groups.

In contrast, CT-based samples are mostly characterized by a much lower moisture loss (Fig. 8b), which indicates a much weaker hydrophilic character. This must be due to a negligible surface density of the hydroxyl groups on the commercial untreated CT. Polyol incorporation allowed to overcome this drawback by introducing hydrophilic OH groups, as reflected by the noticeable increase in the moisture content from *ca.* 0.1% up to 0.277% (Table 1).

Further incorporation of MNP in CT or in H20–CT induced a marked enhancement of the hydrophilic character. This is supported by more pronounced WL in the temperature range of 47–200 °C up to 8.25% (Cu^0/CT), 9.74% (Ag^0/CT), 4.675% (Cu^0/H20–CT), and 8.525% (Ag^0/H20–CT) (Table 2). Here, in spite of the competitive [–HO:Metal] and [–HO:H_2O] interactions, the mere presence of OH groups in the vicinity of MNP seems to enhance the surface affinity toward water.[53] This confirms the narrow interdependence between the moisture content that reflects that the hydrophilic character is expected to favor material dispersion in aqueous media and surface basicity that promotes metal retention.

3.6. Evidence of metal retention on the clay surface

Evidence of metal dispersion in NaMt was provided by X-ray photoelectron spectroscopy. Changes in the binding energy (BE) of the electrons belonging to the material atoms before and after metal dispersion are expected to provide valuable information about the MNP retention strength and subsequently the antibacterial activity. The values of BE shift are considered as being proportional to the interaction strength. Metal incorporation in NaMt was revealed by new XPS signals, *i.e.*, Cu $2p_{3/2}$ at 931.42 eV for Cu^0/NaMt and Ag $3d_{5/2}$ at 367.99 eV for Ag^0/NaMt (Table 2). Other signals for Cu $2p_{1/2}$ at 953.00 eV and Ag $3d_{3/2}$ at 373.89 eV provide confirmation of the presence of Cu^0 and Ag^0 particles. No loss feature was detected between Ag $3d_{5/2}$ and Ag $3d_{3/2}$ and for higher BE, suggesting the occurrence of Ag^+ cations and the incomplete reduction by $NaBH_4$, in agreement with the SEM data.

A weak satellite was barely detected at about 943.50 eV, indicating the presence of trace amounts of Cu_2O. The C 1s signals at 285.05 eV for NaMt and at 285.03 eV for Cu^0/NaMt were both assigned to the O–C=O groups, and indicate the presence of carbonates (CO_3^{2-}), as supported by the XRD pattern of bentonite with 113, 202, and 018 plane families between 40 and 45° (Fig. S8†). The marked BE increase of the C 1s signal for Ag/NaMt from 285.05 to 289.49 suggests a strong interaction between carbonate and silver, presumably through the formation of metal carbonate.

3.7. Role of oxygen atom in metal–clay interaction

The most important XPS results reside in the shifts of the binding energy (BE) of the key elements (oxygen, silicon, and aluminum), providing evidence of the occurrence of metal interaction with the host surface. For oxygen, the BE value decreased from 532.66 eV down to 531.48 eV and 531.59 eV

Table 2 Binding energy (eV) shifts for key elements in the synthesized materials

				Binding energy (eV)					
	Theoretical data			**NaMt**			**Cellulose tissue (CT)**		
Electron type	Matrix/group	Alone	Alone	+Cu^0	+Ag^0	Alone	+H20	+Cu^0/H20	+Ag^0/H20
O 1s	SiO_2	532.9[a]	532.60	531.48	531.59	532.71	532.71	531.65	531.74
	Al_2O_3	531.1	—	—	—	—	—	—	—
	C=O	531.5	—	—	—	—	—	531.65	531.74
	C–O–H	532.9	—	—	—	—	—	533.54	533.66
	Unknown	—	—	—	—	—	—	536.11	535.85
C 1s	C–C	284.8[b]	—	—	—	285.05	285.01	281.61	285
	C–O–C	286[c]	—	—	—	286.45	286.16	282.96	—
	O–C=O	288.5	285.05	285.03	289.49	288.98	288.96	285.71	—
Al 2p	Aluminosilicate	74.4[b]	75.25	76.00 (low)	74.99	—	—	—	—
Si 2s	SiO_2	149	154.55	152.00	149	—	—	—	—
Si 2p	SiO_2	103.5	103.25	103.00	103.4	—	—	—	—
	Alumino-silicate	102.7	103.55			—	—	—	—
Ag $3d_{5/2}$[a]		368.2	—	—	367.99	—	—	—	368
Ag $3d_{3/2}$[a]		374.5	—	—	373.89	—	—	—	368
Cu $2p_{3/2}$[b]		933	—	931.42	—	932.65	—	932.97	—
Cu $2p_{1/2}$[b]		952.5	—	953.00	—	—	—	940	—
Cu satellite			943.50						

[a] XPS data for silver metal: Ag $3d_{5/2}$ = 368.2 eV. [b] XPS data for copper metal: Cu $2p_{3/2}$ = 933 eV.

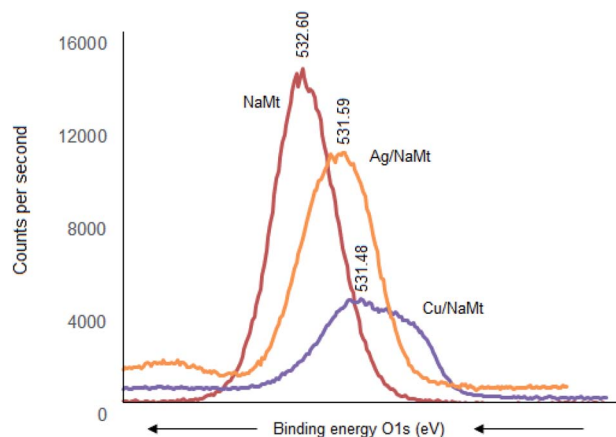**Fig. 5** XPS signals for O 1s electrons in NaMt and metal-loaded counterparts.

upon Cu^0 and Ag^0 incorporation, respectively. The larger BE shift of the O 1s signal for Cu/NaMt suggests stronger Cu^0 retention by the clay surface as compared to Ag^0 (Fig. 5). Such a BE weakening indicates an attraction by next-neighboring species, and can be explained in terms of Lewis-acid–base (LAB) interaction between clay lattice oxygens and MNP. The stronger [Clay–O:Cu^0] interaction was also reflected by a wider and asymmetric O 1s signal for Cu/NaMt, as compared to Ag/NaMt.

Signal deconvolution of this asymmetric signal for Cu/NaMt revealed three partially overlapped O 1s signals, presumably due to multiple Cu^0 interactions with at least in-plane and out-of-plane silanols, with Si–O–Si groups and to a lesser extent with Al–OH groups (aluminol). This somehow explains the higher dispersion of Cu^0 on NaMt as compared to Ag^0. Confirmation in this regard was provided by BE decrease for Si 2s electrons from 154.55 eV to 152 eV but slight Al 2p BE increase from 75.25 eV to

76.00 eV after Cu^0 incorporation. This indicates that Al–OH interaction with CuNP, if any, should have only weak contribution to copper retention. Interestingly, Ag^0 incorporation produced more pronounced Si 2s BE decrease from 154.55 eV down to 149 eV but barely detectable Al 2p shift from 75.25 eV to 74.99 eV. This is a precise indicator of the occurrence of stronger [Ag^0:Si] interaction without necessarily favoring silver dispersion on NaMt, as compared to Cu^0, but almost negligible interaction with Al atoms.

3.8. Metal interaction in organic matrices

CT, H20, and their H20–CT composite showed XPS similar patterns with similar C 1s signals at 288.91, 286.41, and 285.11 eV, attributed to O–C═O, C–O–C, and CC-groups, respectively (Fig. 6). The intensity of each C 1s signal for H20-CT appears to be the sum of those of both organic components. No BE shift was detected, suggesting that CT interaction with H20, if any, should be negligible.

Cu^0 incorporation also induced no C 1s BE shift in CT (Fig. 7a) but a pronounced BE decrease down to 285.71, 282.81, and 281.61 eV, respectively (Fig. 7b). Similar sequence was registered after AgNP insertion, providing evidence of strong [AgNP:H20–CT] interaction through the carbon atoms.

This marked BE shift for the C 1s signal of more than 3 eV compared to the almost total lack of BE shift in CT alone accounts for a higher capacity of H20–CT toward host MNP (Fig. 6). This is due to the contribution of the dendritic entanglement. The noticeable intensity decrease for the C 1s signal of C–O–C and C–C groups (Fig. 7b) suggests a compaction of the dendritic entanglement around MNPs.

3.9. Role of oxygen atom in metal–polymer interaction

Metal–matrix interaction should also involve the oxygen atoms of the polymers. No H-bridges seem to arise between CT and dendrimer H20, given the absence of a detectable shift of the O 1s signal at 532.71 eV (Fig. 8a). Nonetheless, CT was found to interact with the incorporated Cu as supported by the O 1s shift from 532.7 to 531.91 eV and the appearance of a new signal at 533.31 eV was assigned to the –C–O–H group (Fig. 8b). This is presumably due to the increase in [–HO:Cu] interaction.

A BE shift from 532.56 eV down to 531.81 and a signal widening were observed after Cu^0 incorporation in the dendrimer H20 alone (Fig. 9a). The slightly higher BE decrease from 532.56 eV down to 531.71 eV registered after Ag^0 incorporation indicates a paradoxically stronger interaction of silver with the oxygen atoms of the dendrimer. Similar signal widening at about 532.70 eV was observed for Cu^0/H20–CT with the appearance of a second signal at 534.31 eV attributed to the –C–O–H group (Fig. 9b). Surprisingly, the higher density of hydroxyl groups in H20 as compared to CT gave only a slightly higher signal. This may be due to signal mitigation by the effect of H20 entanglement compaction.[27–29] Here, the [–HO:MNP] interaction strength is expected to determine the entanglement compaction or, in contrast, the MNP release according to the pH changes in the aqueous media.
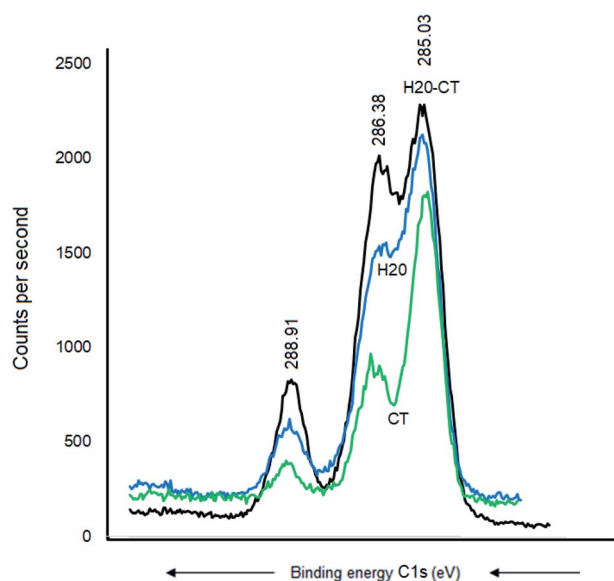

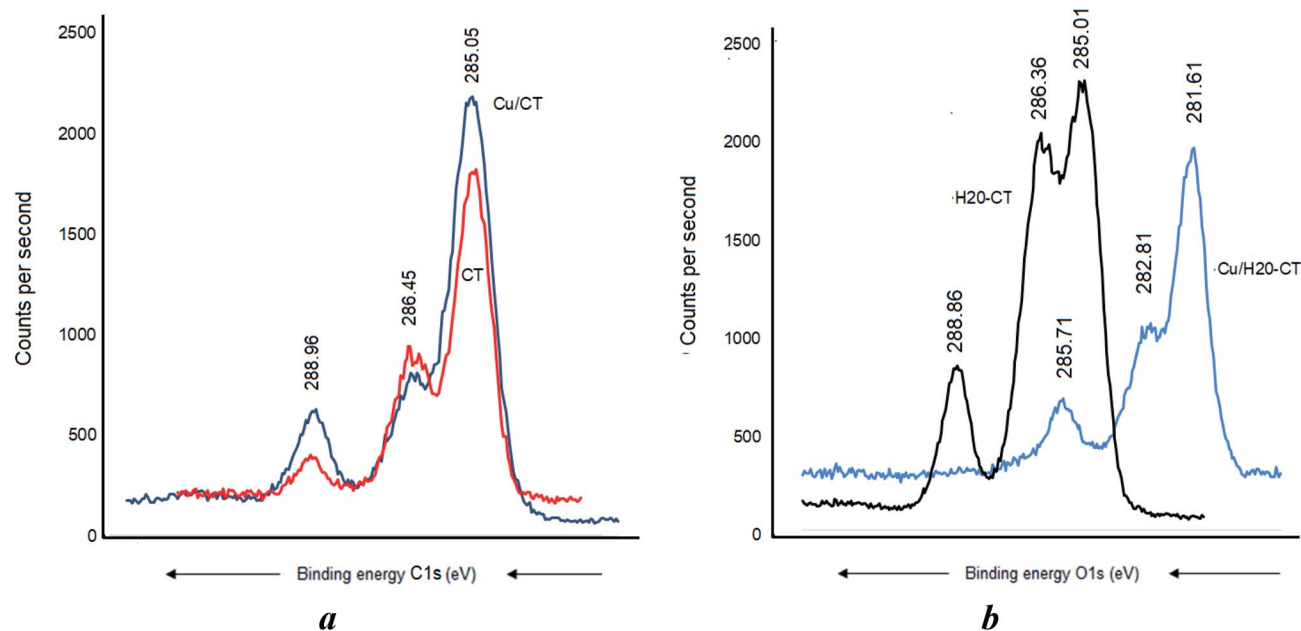**Fig. 6** C 1s XPS signals for metal-free CT, H20, and H20–CT.

Fig. 7 C 1s XPS signals for Cu-loaded CT (a) and Cu-loaded H20−CT (b).

3.10. Antibacterial activity of metal-loaded NaMt

Triplicate incubation tests at 37 °C for 24 h of 74×10^6 CFU mL^{-1} populations of *E. coli* and *B. subtilis* strains revealed no antibacterial activity in the presence of metal-free NaMt, dendrimer H20, H20/NaMt, and cellulose tissue. As compared to the starting NaMt, copper- and silver-loaded montmorillonite (Cu^0/NaMt and Ag^0/NaMt) exhibited noticeable antibacterial activity against both the bacterial strains, as illustrated by the marked increase in the diameter of the inhibition zone (Fig. 10). This providing evidence of the beneficial effect of metal incorporation.[54–57] Lower IZD was registered for Cu^0/NaMt (1.40 cm)

as compared to Ag^0/NaMt (1.87 cm) in the presence of *E. coli* but comparable IZD (1.83 cm) were obtained for both Cu^0/NaMt and Ag^0/NaMt in the presence of *B. subtilis* (Table S1†). This suggests a weaker antibacterial effect of CuNP on *E. coli*.

The addition of dendrimer H20 on NaMt induced a visible improvement of the antibacterial activity, as illustrated by a larger inhibition zone (Fig. S10†). This can be explained in terms of higher metal dispersion within the dendrimer entanglement bearing OH groups that act as chelating agents (Lewis base). The higher IZD values registered for Cu^0/H20–NaMt with both strains (1.77 and 1.83 cm *versus* 1.07 and 150 cm for Ag^0/H20–NaMt)
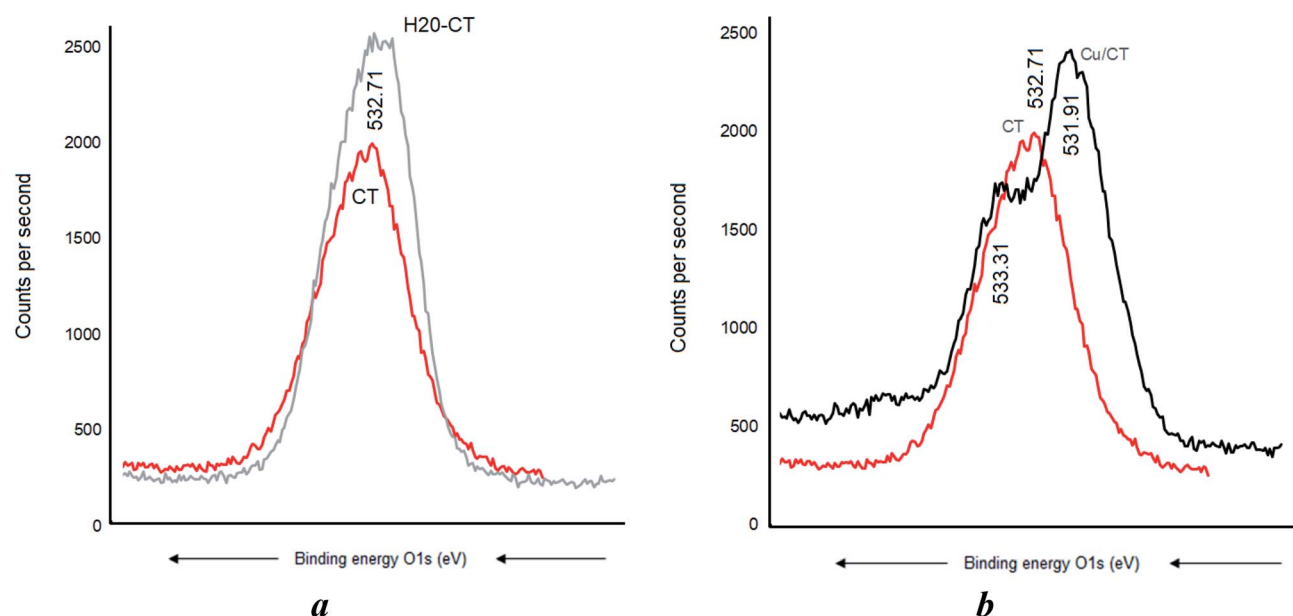

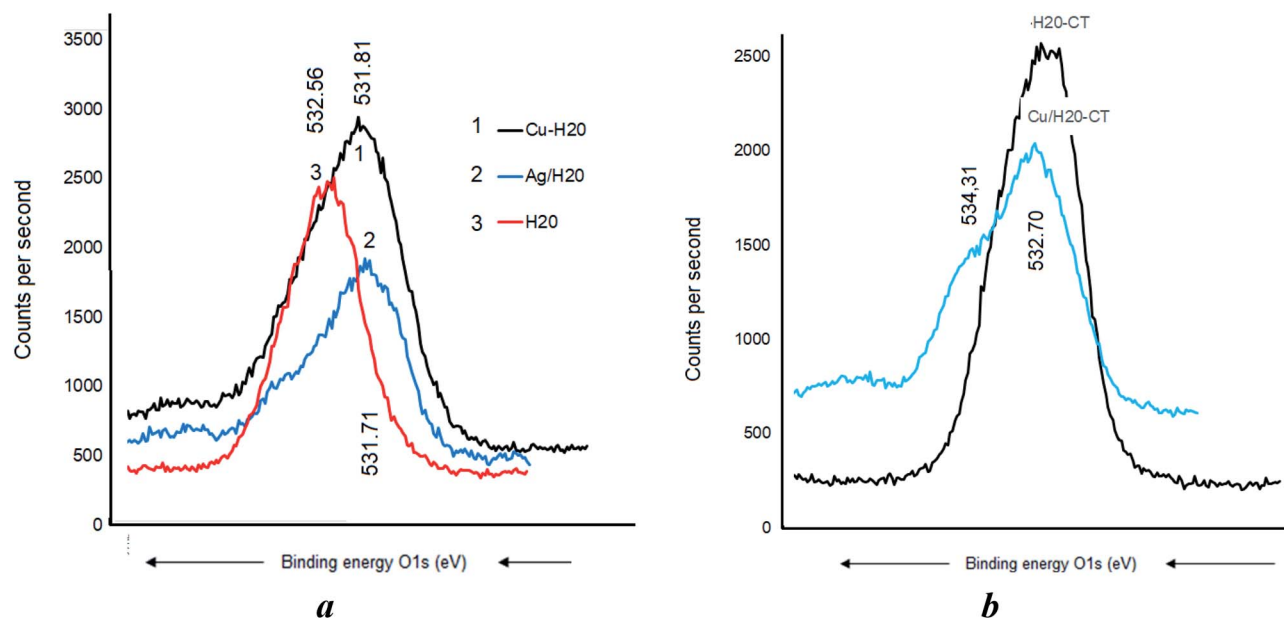**Fig. 8** O 1s XPS signals after CT loading by dendrimer H20 (a) and CuNP (b).

Fig. 9   O 1s signals for O 1s electrons in CT alone (a) and dendrimer H20 alone (b).

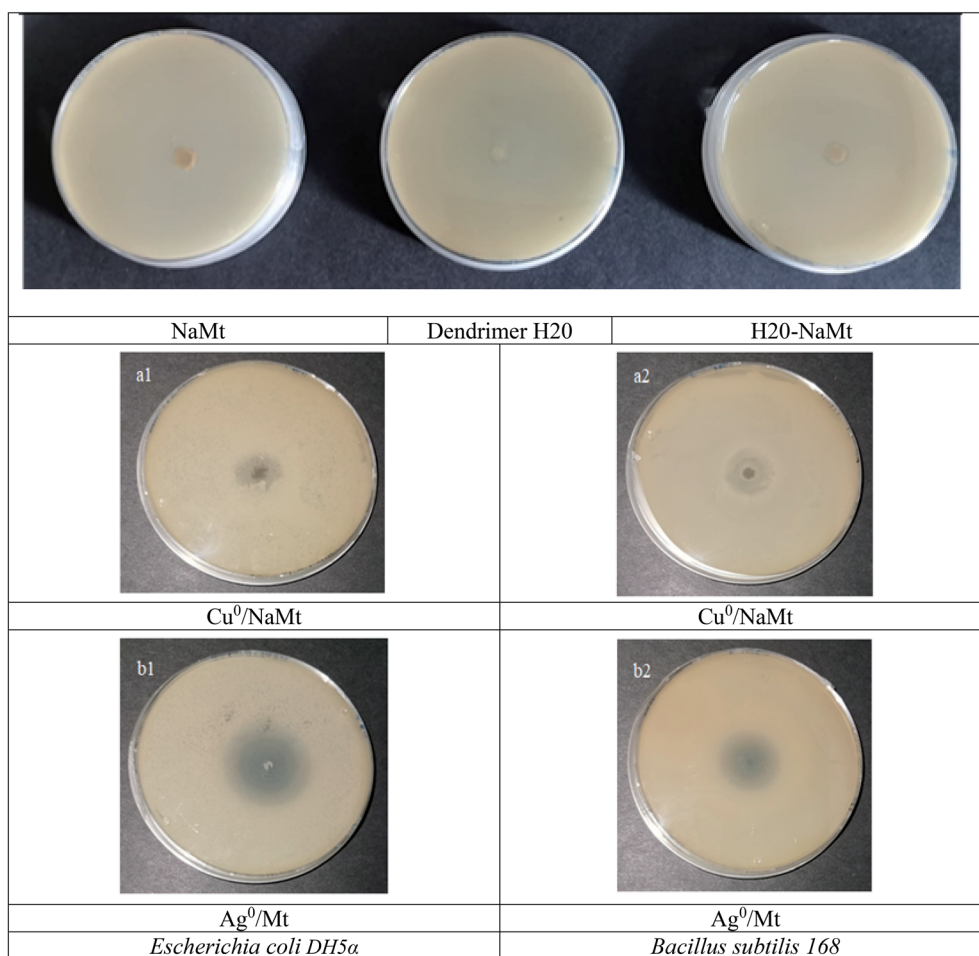**Fig. 10**   Inhibition zones in the proliferation of both bacterial strains in the presence of NaMt and metal-loaded counterparts.

indicate that Cu⁰ is more effective than Ag⁰, presumably due to (i) a higher dispersion by dendrimer H20 as revealed by TEM, and (ii) an easier release of copper in the liquid media as a result of the higher dispersion of the material particles.

Besides, copper is also known to be more reactive than silver, generating oxygen reactive species (ROS) as in Fenton-like and Haber–Weiss processes. Other possible explanations should involve lower amounts of inserted Ag⁰ atoms. This must be due to the lower reduction level of Ag⁺ cations in agreement with the XPS data and the large amount of non-dispersed rod-like silver salt crystals revealed by the SEM images (Fig. 1a). The general tendency is that high antibacterial ability is observed against Gram-positive *B. subtilis*, as illustrated by the largest IZD values (Table S1†). This can be due to the very structure of the *Bacillus* cell wall with a thick peptidoglycan layer and an abundant amount of pores that confers them more sensitivity to reactive species as compared to Gram-negative *E. coli*.[51] The high concordance between the material characterization data and antibacterial activity allows stating that judiciously tailored [metal–matrix] interaction allows the design of effective antibacterial agents.

3.11. Effect of clay dispersion and particle size

The clay dispersion in water is expected to play a key-role in the antibacterial activity because it is assumed to improve the contact surface available for MNP exchange with culture media. Clay material dispersion in water induced specific intrinsic pH levels. A correlation attempt from the data summarized in Table S1† showed that the average particle increased the pH from 6.01 up to 9.28, which resulted in a marked decreased in the particle size from 401.9 down to 127.6 μm (Fig. 11a). This accounts for a significant clay material dispersion in water, most likely due to increasing repulsive forces between the clay lamellae, as supported by an increasing tendency of the negative value of the zeta potential (Fig. 11b). However, the occurrence of a maximum value of 38.12 mV for H20–NaMt indicates that increasing zeta potential is not the sole factor in clay dispersion and that the modified clay structure also plays a role in this regard.

Interestingly, the highest dispersion grade, *i.e.*, the lowest particle sizes were obtained for Ag⁰/H20–NaMt (127.6 nm) and Ag⁰/NaMt (152.7 nm), which displayed moderate zeta potential of −27.21 and −28.31 mV, respectively (Fig. 11c). A possible explanation resides in a much weaker aggregation of clay or organoclay particles around AgNP.

As expected, the particle size was found to exhibit a markedly favorable influence on the antibacterial activity, as supported by the decreasing tendency of the IZD with increasing particle size (Fig. 11d), thereby confirming the previous statement of the key
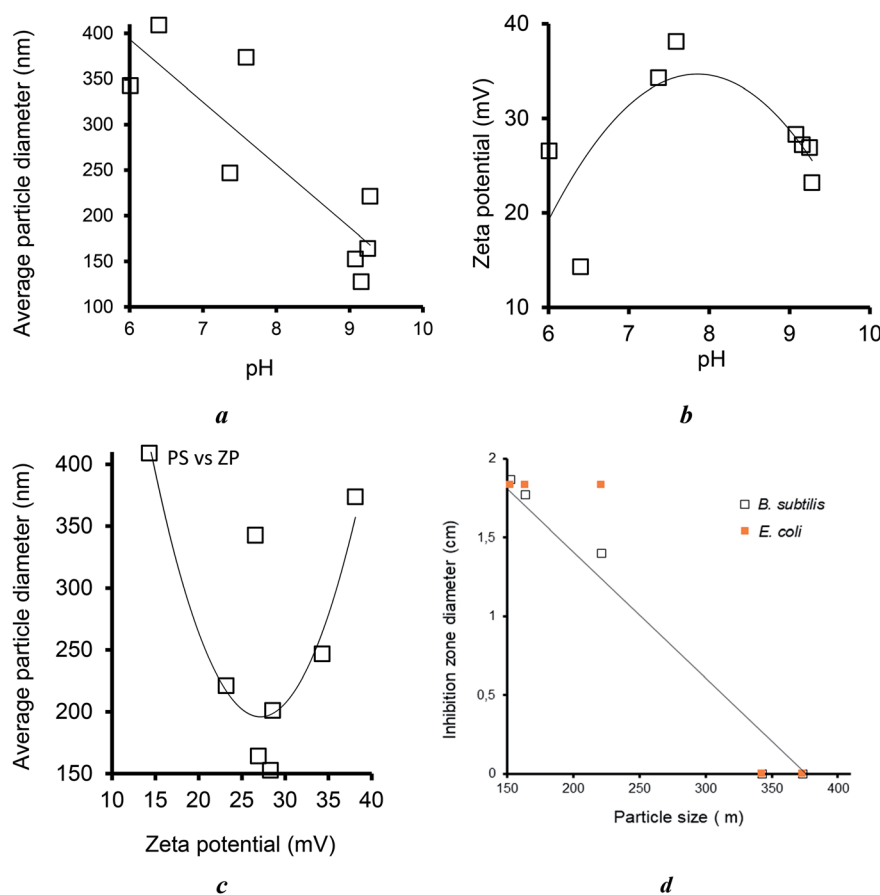

Fig. 11 Effect of pH on the average particle size (a) and zeta potential (b), their interdependence (c), and influence of the particle size on the IZD for both bacterial strains (d).
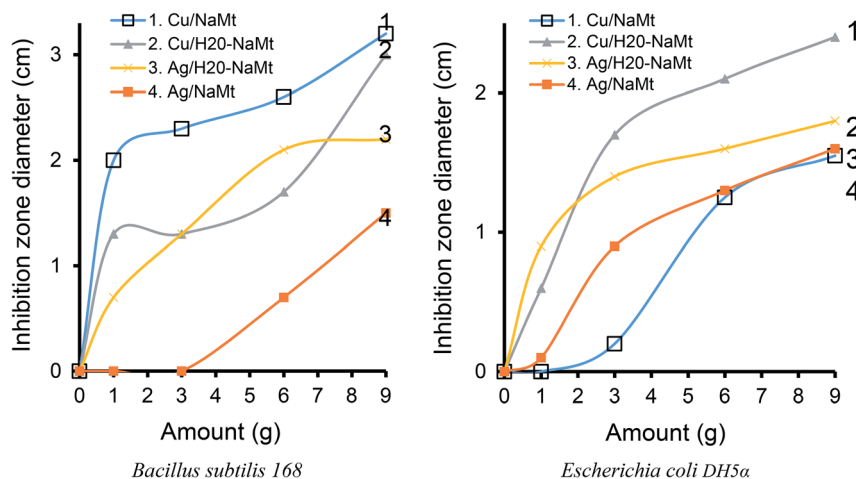
© 2021 The Author(s). Published by the Royal Society of Chemistry

Fig. 12 Effect of the amount of antibacterial material on the inhibition zone diameter in Petri dishes pre-seeded by approximately 74×10^6 colony forming units CFU mL^{-1} of each bacterial species with a cell optical density of 0.5 at 600 nm.

role of the contact surface. This provides additional arguments in favor of the proof-of-concept that an optimal equilibrium between metal retention and release by the host–matrix is a key factor for high antibacterial activity. In other words, strong metal retention improves the carrier capacity of the host–matrix but, paradoxically, easy metal release in the culture media improves the antibacterial activity. This simultaneously requires (i) high metal dispersion and stabilization (fine particle size); (ii) high matrix dispersion (low material particle size) to improve the contact surface; and (iii) tunable metal retention according to the features of the aqueous media.

3.12. Effect of metal amount in the clay samples

One of these features is undoubtedly the amount of incorporated metal, which appears to play a key-role in the effectiveness of the antibacterial agent. Deeper insights through different amounts of metal-loaded organoclays ranging from 1 to 9 mg revealed an almost proportional IZD increase for both the strains, *E. coli* and *B. subtilis*, with increasing amounts of bactericidal agents up to a certain level (Fig. 12). Maximal values of 2.5 and 3.5 cm for 9 mg of Cu^{2+}/NaMt–H20 and of 2.4 and 3 cm for the same amount of Cu^0/NaMt–H20 against *E. coli* and *B. subtilis* were respectively obtained (Table S2†).

The general trend is that higher IZD values were obtained with *B. subtilis* as compared to *E. coli*. This confirms the previous assertion of the higher sensitivity of *Bacillus subtilis*.[51] It is also worth mentioning that Cu^0/NaMt showed highest IZD values for *Bacillus subtilis 168* but lowest values for *E. Coli*, in agreement with the previous data (Table S1†).

3.13. Effect of the solid surface

In order to investigate the role of the solid support, similar antibacterial tests performed with cellulose-based samples against both *E. coli* and *B. subtilis* revealed the absence of antibacterial activity for cellulose tissue (CT) and its polyol-functionalized counterpart (H20–CT). In contrast, Cu-loaded cellulose matrices exhibited strong activity against the

bacteria, as illustrated by the significant IZD increase (Table 3). This a clear confirmation that the antibacterial activity is only due to metal incorporation regardless of the host–matrix. The highest IZD values obtained for Cu^0/H20–CT (3.5 cm) must be due to both the beneficial role of dendrimer H20 and higher antibacterial activity of copper as compared to silver. Interestingly, this value is higher than those of 2.23 cm for *E. coli* and 2.73 cm for *B. subtilis* registered in the presence of Cu^{2+}/H20–NaMt (Table S1†). Similar observations were made for Ag^0/H20–NaMt with a 0.90 cm IZD *versus* 2 cm for Ag^0/H20@CT.

The most plausible explanation resides in a higher metal dispersion in the CT samples by all the hydroxyls of dendrimer H20. Indeed, unlike on montmorillonite, the OH groups of H20 are expected to preponderantly interact with MNP at the expense of the H-bridges with a negligible amount of OH on the CT surface, as supported by the TPD measurements (Fig. S7b†). This somehow explains the total absence of H20–CT interaction, in agreement with the XPS data. This result is of great importance because it clearly demonstrates that the interaction of the polyol dendrimer with the solid surface is detrimental for MNP dispersion and antibacterial activity.

The effect of the surface charge and subsequently of the zeta potential on the antibacterial activity should also be taken into

Table 3 Inhibition zone diameter (cm) for metal-loaded CT-based materials

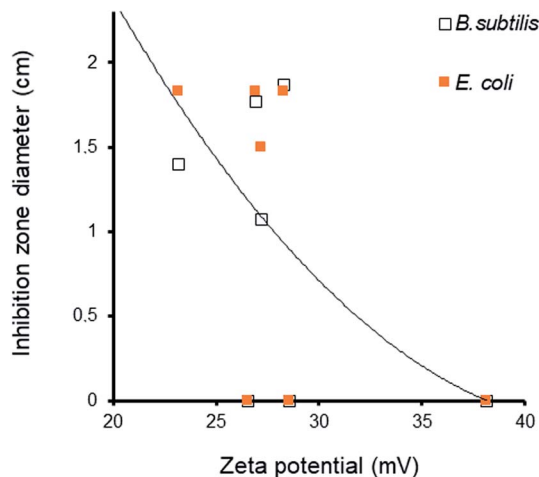| Samples	Inhibition zone diameter (cm)	
	B. subtilis 168	*E. coli DH5α*
CT	0	0
Boltorn™ H20	0	0
H20@CT	0	0
Ag^0/CT	1	0
Cu^0/CT	1.6	0.5
Cu^0/H20@CT	3.5	1
Ag^0/H20@CT	2	0.9

Fig. 13 Effect of zeta potential on the IZD for both the bacterial strains.

account. The general tendency is that increased absolute value of the zeta potential induced a marked decay in the antibacterial activity, as well illustrated by the visible IZD decrease (Fig. 13). This suggests a detrimental effect to a higher density of negative charge on the solid surface that impedes [material:bacteria wall] interaction through repulsive forces. The external side of the cell wall of both Gram-positive and Gram-negative bacteria bears negative charges.[58,59]

Unlike with cations, negatively charged bacterial cell walls do not interact with negatively charged particles due to repulsive electrostatic forces. Decreasing zeta potential is supposed to improve bacterial contact with the solid surface, MNP release due to attractive Lewis base sites of the cell wall, and further diffusion inside the cell.[59] Inside the cell, MNP can generate reactive oxygen species (ROS) such as hydrogen peroxide (H_2O_2, superoxide anion ($^\bullet O_2^-$), and hydroxyl radical $^\bullet OH$[56,57] that alter the cell stability[60] *via* a wide variety of processes against bacteria.[60–62] In spite of their antibacterial activity,[63] AgNP were found to be less effective than cations,[64] which are much more attracted by the negative charges of the bacterial walls.[56,62,65] Similar observations can be made for CuNP,[66,67] whose concentration and dissolution in the bacterial membrane is known to induce potential and permeability changes, membrane alteration,[68,69] production of ROS and other detrimental oxidative processes,[70,71] decay in intracellular ATP production, and disruption of DNA replication[13,72] This should confer higher activity to CuNP against both the bacteria compared to AgNP,[73] thereby explaining the higher performance of polyol-dispersed copper reported herein.

4. Conclusion

Metal dispersion in the form of AgNP and CuNPs with polyol dendrimer induced antibacterial activity on montmorillonite and cellulose tissue. Previous polyol incorporation induced no detectable antibacterial activity but provided additional hydroxyl groups that act as chelating agents for MNP. Strong [–HO:metal] interaction reduces MNP accessibility and affects the antibacterial activity. Weak -[–HO:metal] interaction attenuates MNP retention and promotes the antibacterial activity. Optimal amount of metal-loaded polyol composites results in high biocidal effect through a compromise between structure compaction and MNP accessibility to the bacterial cells. Polyol dendrimer interaction with the solid surface appears to be detrimental for MNP dispersion. High antibacterial activity involves a judicious compromise between strong metal retention to improve the carrier capacity of the host–matrix and easy metal release in the culture media. This requires high dispersion and low size of both the metal particles and material grains to improve the contact surface. Tunable metal retention according to the features of the aqueous media appears to be a key factor in this regard. The higher density of negative charge on the solid surface impedes [material:bacterial wall] interaction through repulsive forces. These findings are essential requirements for designing effective antibacterial matrices with natural and low-cost materials with tunable entanglement porosity.

Author contributions

Farzaneh Noori: investigation, data curation, writing – original draft preparation, Armelle Tchoumi Neree: investigation, data curation, Meriem Megoura: investigation, data curation, Mircea Alexandru Mateescu: supervision, conceptualization, methodology, writing – reviewing and editing, Abdelkrim Azzouz: supervision, conceptualization, methodology, writing – reviewing and editing, corresponding author.

Conflict of interests

There are no conflicts to declare.

Acknowledgements

References

1 S. B. Levy, The challenge of antibiotic resistance, *Sci. Am.*, 1998, **278**, 46–53.

2 G. M. Cragg and D. J. Newman, Natural products: a continuing source of novel drug leads, *Biochim. Biophys. Acta, Gen. Subj.*, 2013, **1830**, 3670–3695.

3 S. Martin and W. Griswold, Human health effects of heavy metals, *Environmental Science and Technology Briefs for Citizens*, 2009, **15**, 1–6.

4 M. Rai, A. Yadav and A. Gade, Silver nanoparticles as a new generation of antimicrobials, *Biotechnol. Adv.*, 2009, **27**, 76–83.

5 M. I. Carretero, Clay minerals and their beneficial effects upon human health. A review, *Appl. Clay Sci.*, 2002, **21**, 155–163.

6   A. Gupta, M. Maynes and S. Silver, Effects of halides on plasmid-mediated silver resistance in *Escherichia coli*, *Appl. Environ. Microbiol.*, 1998, **64**, 5042–5045.

7   G. Čík, H. Bujdáková and F. Šeršeň, Study of fungicidal and antibacterial effect of the Cu(II)-complexes of thiophene oligomers synthesized in ZSM-5 zeolite channels, *Chemosphere*, 2001, **44**, 313–319.

8   G. Čík, S. Priesolová, H. Bujdáková, F. Šeršeň, T. Potheöová and J. Krištín, Inactivation of bacteria G+-S. aureus and G-
-E. coli by phototoxic polythiophene incorporated in ZSM-5 zeolite, *Chemosphere*, 2006, **63**, 1419–1426.

9   C. Costa, A. Conte, G. G. Buonocore and M. A. Del Nobile, Antimicrobial silver-montmorillonite nanoparticles to prolong the shelf life of fresh fruit salad, *Int. J. Food Microbiol.*, 2011, **148**, 164–167.

10 P. Herrera, R. Burghardt and T. Phillips, Adsorption of Salmonella enteritidis by cetylpyridinium-exchanged montmorillonite clays, *Vet. Microbiol.*, 2000, **74**, 259–272.

11 B. Dizman, J. C. Badger, M. O. Elasri and L. J. Mathias, Antibacterial fluoromicas: a novel delivery medium, *Appl. Clay Sci.*, 2007, **38**, 57–63.

12 V. A. A. España, B. Sarkar, B. Biswas, R. Rusmin and R. Naidu, Environmental applications of thermally modified and acid activated clay minerals: current status of the art, *Environ. Technol. Innovation*, 2019, **13**, 383–397.

13 J. S. Kim, E. Kuk, K. N. Yu, J.-H. Kim, S. J. Park, H. J. Lee, S. H. Kim, Y. K. Park, Y. H. Park and C.-Y. Hwang, Antimicrobial effects of silver nanoparticles, *Nanomedicine*, 2007, **3**, 95–101.

14 B. Nabil, C. Christine, V. Julien and A. Abdelkrim, Polyfunctional cotton fabrics with catalytic activity and antibacterial capacity, *Chem. Eng. J.*, 2018, **351**, 328–339.

15 F. Noori, N.-A. Tchoumi, M. Megoura, M. A. Mateescu and A. Azzouz, *Metal-loaded porous polyhydroxylic matrices with improved antibacterial properties*, Authorea Preprints, 2020.

16 N. V. Rees, Y. G. Zhou and R. G. Compton, The aggregation of silver nanoparticles in aqueous solution investigated *via* anodic particle coulometry, *ChemPhysChem*, 2011, **12**, 1645–1647.

17 P. Biegański, Ł. Szczupak, M. Arruebo and K. Kowalski, Brief survey on organometalated antibacterial drugs and metal-based materials with antibacterial activity, *RSC Chem. Biol.*, 2021, **2**, 368–386.

18 R. M. Crooks, M. Zhao, L. Sun, V. Chechik and L. K. Yeung, Dendrimer-encapsulated metal nanoparticles: synthesis, characterization, and applications to catalysis, *Acc. Chem. Res.*, 2001, **34**, 181–190.

19 J. Hellmann, M. Hamano, O. Karthaus, K. Ijiro, M. Shimomura and M. Irie, Aggregation of dendrimers with a photochromic dithienylethene core group on the mica surface-atomic force microscopic imaging, *Jpn. J. Appl. Phys.*, 1998, **37**, L816.

20 P. Bragg and D. Rainnie, The effect of silver ions on the respiratory chain of *Escherichia coli*, *Can. J. Microbiol.*, 1974, **20**, 883–889.

21 P. Komadel, Acid activated clays: materials in continuous demand, *Appl. Clay Sci.*, 2016, **131**, 84–99.

22 M. Nadziakiewicza, S. Kehoe and P. Micek, Physico-Chemical Properties of Clay Minerals and Their Use as a Health Promoting Feed Additive, *Animals*, 2019, **9**, 714.

23 L. B. Williams, D. W. Metge, D. D. Eberl, R. W. Harvey, A. G. Turner, P. Prapaipong and A. T. Poret-Peterson, What makes a natural clay antibacterial?, *Environ. Sci. Technol.*, 2011, **45**, 3768–3773.

24 A. Stavitskaya, S. Batasheva, V. Vinokurov, G. Fakhrullina, V. Sangarov, Y. Lvov and R. Fakhrullin, Antimicrobial applications of clay nanotube-based composites, *Nanomaterials*, 2019, **9**, 708.

25 A. Roy, M. Joshi and B. S. Butola, Antimicrobial performance of polyethylene nanocomposite monofilaments reinforced with metal nanoparticles decorated montmorillonite, *Colloids Surf., B*, 2019, **178**, 87–93.

26 A. Azzouz, S. Nousir, N. Bouazizi and R. Roy, Metal–inorganic–organic matrices as efficient sorbents for hydrogen storage, *ChemSusChem*, 2015, **8**, 800–803.

27 M. N. Tahir, R. Sennour, V. A. Arus, L. M. Sallam, R. Roy and A. Azzouz, Metal organoclays with compacted structure for truly physical capture of hydrogen, *Appl. Surf. Sci.*, 2017, **398**, 116–124.

28 R. Sennour, T. C. Shiao, V. A. Arus, M. N. Tahir, N. Bouazizi, R. Roy and A. Azzouz, Cu 0-Loaded organo-montmorillonite with improved affinity towards hydrogen: an insight into matrix–metal and non-contact hydrogen–metal interactions, *Phys. Chem. Chem. Phys.*, 2017, **19**, 29333–29343.

29 A. V. Arus, M. N. Tahir, R. Sennour, T. C. Shiao, L. M. Sallam, I. D. Nistor, R. Roy and A. Azzouz, Cu^0 and Pd^0 loaded Organo-Bentonites as Sponge-like Matrices for Hydrogen Reversible Capture at Ambient Conditions, *ChemistrySelect*, 2016, **1**, 1452–1461.

30 A. Azzouz, E. Assaad, A.-V. Ursu, T. Sajin, D. Nistor and R. Roy, Carbon dioxide retention over montmorillonite–dendrimer materials, *Appl. Clay Sci.*, 2010, **48**, 133–137.

31 C.-N. H. Thuc, A.-C. Grillet, L. Reinert, F. Ohashi, H. H. Thuc and L. Duclaux, Separation and purification of montmorillonite and polyethylene oxide modified montmorillonite from Vietnamese bentonites, *Appl. Clay Sci.*, 2010, **49**, 229–238.

32 A. Azzouz, D. Nistor, D. Miron, A. Ursu, T. Sajin, F. Monette, P. Niquette and R. Hausler, Assessment of acid–base strength distribution of ion-exchanged montmorillonites through NH_3 and CO_2-TPD measurements, *Thermochim. Acta*, 2006, **449**, 27–34.

33 I. Terrab, B. Boukoussa, R. Hamacha, N. Bouchiba, R. Roy, A. Bengueddach and A. Azzouz, Insights in CO_2 interaction on zeolite omega-supported polyol dendrimers, *Thermochim. Acta*, 2016, **624**, 95–101.

34 A.-P. Beltrao-Nunes, R. Sennour, V.-A. Arus, S. Anoma, M. Pires, N. Bouazizi, R. Roy and A. Azzouz, CO_2 capture by coal ash-derived zeolites-roles of the intrinsic basicity and hydrophilic character, *J. Alloys Compd.*, 2019, **778**, 866–877.

35 V. A. Arus, S. Nousir, R. Sennour, T. C. Shiao, I. D. Nistor, R. Roy and A. Azzouz, Intrinsic affinity of acid-activated

bentonite towards hydrogen and carbon dioxide, *Int. J. Hydrogen Energy*, 2018, **43**, 7964–7972.

36 A. Azzouz, V.-A. Aruș, N. Platon, K. Ghomari, I.-D. Nistor, T. C. Shiao and R. Roy, Polyol-modified layered double hydroxides with attenuated basicity for a truly reversible capture of CO_2, *Adsorption*, 2013, **19**, 909–918.

37 A. Azzouz, S. Nousir, N. Platon, K. Ghomari, G. Hersant, J.-Y. Bergeron, T. C. Shiao, R. Rej and R. Roy, Preparation and characterization of hydrophilic organo-montmorillonites through incorporation of non-ionic polyglycerol dendrimers derived from soybean oil, *Mater. Res. Bull.*, 2013, **48**, 3466–3473.

38 A. Azzouz, S. Nousir, N. Platon, K. Ghomari, T. C. Shiao, G. Hersant, J.-Y. Bergeron and R. Roy, Truly reversible capture of CO_2 by montmorillonite intercalated with soya oil-derived polyglycerols, *Int. J. Greenhouse Gas Control*, 2013, **17**, 140–147.

39 A. Azzouz, N. Platon, S. Nousir, K. Ghomari, D. Nistor, T. C. Shiao and R. Roy, OH-enriched organo-montmorillonites for potential applications in carbon dioxide separation and concentration, *Sep. Purif. Technol.*, 2013, **108**, 181–188.

40 K. Ghomari, A. Benhamou, R. Hamacha, A. Bengueddach, S. Nousir, T. C. Shiao, R. Roy and A. Azzouz, TPD and DSC insights in the basicity of MCM-48-like silica and modified counterparts, *Thermochim. Acta*, 2015, **600**, 52–61.

41 K. Ghomari, B. Boukoussa, R. Hamacha, A. Bengueddach, R. Roy and A. Azzouz, Preparation of dendrimer polyol/mesoporous silica nanocomposite for reversible CO_2 adsorption: effect of pore size and polyol content, *Sep. Sci. Technol.*, 2017, **52**, 2421–2428.

42 S. Nousir, V.-A. Arus, T. C. Shiao, N. Bouazizi, R. Roy and A. Azzouz, Organically modified activated bentonites for the reversible capture of CO_2, *Microporous Mesoporous Mater.*, 2019, **290**, 109652.

43 S. Nousir, K. Ghomari, R. Roy and A. Azzouz, Polyol-clay matrices with improved hydrophilic character and affinity towards CO_2-Attempts to CO_2 concentration at room temperature, in: *Technical Proceedings of the 2013 NSTI Nanotechnology Conference and Expo*, NSTI-Nanotech, Washington D. C. USA, 2013, pp. 197–200.

44 S. Nousir, N. Platon, K. Ghomari, A.-S. Sergentu, T. C. Shiao, G. Hersant, J.-Y. Bergeron, R. Roy and A. Azzouz, Correlation between the hydrophilic character and affinity towards carbon dioxide of montmorillonite-supported polyalcohols, *J. Colloid Interface Sci.*, 2013, **402**, 215–222.

45 S. Nousir, A.-S. Sergentu, T. C. Shiao, R. Roy and A. Azzouz, Hybrid Clay Nanomaterials with Improved Affinity for Carbon Dioxide through Chemical Grafting of Amino Groups, *Int. J. Environ. Pollut. Rem.*, 2014, **2**, 59–65.

46 S. Nousir, G. Yemelong, S. Bouguedoura, Y. M. Chabre, T. C. Shiao, R. Roy and A. Azzouz, Improved carbon dioxide storage over clay-supported perhydroxylated glucodendrimer, *Can. J. Chem.*, 2017, **95**, 999–1007.

47 I. Grün and K. Dirr, The differentiation of pathogenic and nonpathogenic staphylococci by estimation of the reduction of amido-blue-black and methylene blue, *Int. J. Syst. Evol. Microbiol.*, 1967, **17**, 391–394.

48 B. Lorenz, N. Ali, T. Bocklitz, P. Rösch and J. Popp, Discrimination between pathogenic and non-pathogenic *E. coli* strains by means of Raman microspectroscopy, *Anal. Bioanal. Chem.*, 2020, **412**, 8241–8247.

49 A. Behrouzi, F. Vaziri, F. R. Rad, A. Amanzadeh, A. Fateh, A. Moshiri, S. Khatami and S. D. Siadat, Comparative study of pathogenic and non-pathogenic *Escherichia coli* outer membrane vesicles and prediction of host-interactions with TLR signaling pathways, *BMC Res. Notes*, 2018, **11**, 1–7.

50 M. Sulpizi, M. P. Gaigeot and M. Sprik, The Silica–Water Interface: How the Silanols Determine the Surface Acidity and Modulate the Water Properties, *J. Chem. Theory Comput.*, 2012, **8**, 1037–1047.

51 F. Fu, L. Li, L. Liu, J. Cai, Y. Zhang, J. Zhou and L. Zhang, Construction of cellulose based ZnO nanocomposite films with antibacterial properties through one-step coagulation, *ACS Appl. Mater. Interfaces*, 2015, **7**, 2597–2606.

52 N. Bouazizi, D. Barrimo, S. Nousir, R. B. Slama, R. Roy and A. Azzouz, Montmorillonite-supported Pd^0, Fe^0, Cu^0 and Ag^0 nanoparticles: properties and affinity towards CO_2, *Appl. Surf. Sci.*, 2017, **402**, 314–322.

53 S.-B. Zhu, Interactions of water, ions, and atoms with metal surfaces, *Surf. Sci.*, 1995, **329**, 276–284.

54 M. Vincent, R. E. Duval, P. Hartemann and M. Engels-Deutsch, Contact killing and antimicrobial properties of copper, *J. Appl. Microbiol.*, 2018, **124**, 1032–1046.

55 C. Potera, Understanding the germicidal effects of silver nanoparticles, *Environ. Health Perspect.*, 2012, **120**, a386.

56 L. C. Yun'an Qing, R. Li, G. Liu, Y. Zhang, X. Tang, J. Wang, H. Liu and Y. Qin, Potential antibacterial mechanism of silver nanoparticles and the optimization of orthopedic implants by advanced modification technologies, *Int. J. Nanomed.*, 2018, **13**, 3311.

57 O. Gordon, T. V. Slenters, P. S. Brunetto, A. E. Villaruz, D. E. Sturdevant, M. Otto, R. Landmann and K. M. Fromm, Silver coordination polymers for prevention of implant infection: thiol interaction, impact on respiratory chain enzymes, and hydroxyl radical induction, *Antimicrob. Agents Chemother.*, 2010, **54**, 4208–4218.

58 D. A. Ashmore, A. Chaudhari, B. Barlow, B. Barlow, T. Harper, K. Vig, M. Miller, S. Singh, E. Nelson and S. Pillai, Evaluation of *E. coli* inhibition by plain and polymer-coated silver nanoparticles, *Rev. Inst. Med. Trop. Sao Paulo*, 2018, **60**, 1–11.

59 M. C. Stensberg, Q. Wei, E. S. McLamore, D. M. Porterfield, A. Wei and M. S. Sepúlveda, Toxicological studies on silver nanoparticles: challenges and opportunities in assessment, monitoring and imaging, *Nanomedicine*, 2011, **6**, 879–898.

60 T. Dakal, A. Kumar, R. Majumdar and V. Yadav, Mechanistic basis of antimicrobial actions of silver nanoparticles, *Front. Microbiol.*, 2016, **7**, 1831.

61 P. Yuan, X. Ding, Y. Y. Yang and Q. H. Xu, Metal nanoparticles for diagnosis and therapy of bacterial infection, *Adv. Healthcare Mater.*, 2018, **7**, 1701392.

62 C. Losasso, S. Belluco, V. Cibin, P. Zavagnin, I. Mičetić, F. Gallocchio, M. Zanella, L. Bregoli, G. Biancotto and A. Ricci, Antibacterial activity of silver nanoparticles: sensitivity of different Salmonella serovars, *Front. Microbiol.*, 2014, **5**, 218–227.

63 A. Ávalos, A. Haza, D. Mateo and P. Morales, Silver nanoparticles: applications and toxic risks to human health and environment, *Revista Complutense de Ciencias Veterinarias*, 2013, **7**, 1–23.

64 A. M. El Badawy, R. G. Silva, B. Morris, K. G. Scheckel, M. T. Suidan and T. M. Tolaymat, Surface charge-dependent toxicity of silver nanoparticles, *Environ. Sci. Technol.*, 2011, **45**, 283–287.

65 Y. N. Slavin, J. Asnis, U. O. Häfeli and H. Bach, Metal nanoparticles: understanding the mechanisms behind antibacterial activity, *J. Nanobiotechnol.*, 2017, **15**, 65.

66 A. K. Chatterjee, R. Chakraborty and T. Basu, Mechanism of antibacterial activity of copper nanoparticles, *Nanotechnology*, 2014, **25**, 135101.

67 G. Sánchez-Sanhueza, D. Fuentes-Rodríguez and H. Bello-Toledo, Copper Nanoparticles as Potential Antimicrobial Agent in Disinfecting Root Canals. A Systematic Review, *Int. J. Odontostomat.*, 2016, **10**, 547–554.

68 A. Azam, A. S. Ahmed, M. Oves, M. Khan and A. Memic, Size-dependent antimicrobial properties of CuO nanoparticles against Gram-positive and-negative bacterial strains, *Int. J. Nanomed.*, 2012, **7**, 3527–3535.

69 N. A. Amro, L. P. Kotra, K. Wadu-Mesthrige, A. Bulychev, S. Mobashery and G.-y. Liu, High-resolution atomic force microscopy studies of the Escherichia coli outer membrane: structural basis for permeability, *Langmuir*, 2000, **16**, 2789–2796.

70 G. Applerot, J. Lellouche, A. Lipovsky, Y. Nitzan, R. Lubart, A. Gedanken and E. Banin, Understanding the antibacterial mechanism of CuO nanoparticles: revealing the route of induced oxidative stress, *Small*, 2012, **8**, 3326–3337.

71 J. Fang, D. Y. Lyon, M. R. Wiesner, J. Dong and P. J. Alvarez, Effect of a fullerene water suspension on bacterial phospholipids and membrane phase behavior, *Environ. Sci. Technol.*, 2007, **41**, 2636–2642.

72 I. Sondi and B. Salopek-Sondi, Silver nanoparticles as antimicrobial agent: a case study on E. coli as a model for Gram-negative bacteria, *J. Colloid Interface Sci.*, 2004, **275**, 177–182.

73 D. Chudobová and R. Kizek, Nanotechnology in diagnosis, treatment and prophylaxis of infectious diseases, *J. Metallomics Nanotechnol.*, 2015, **2**, 67–69.